University of Tehran

Earth Observation and Geomatics Engineering

Online ISSN: 2588-4360

Homepage: https://eoge.ut.ac.ir/

Anisotropic Behaviour of Atmospheric Disturbances in Coastal Areas for Satellite Radar Interferometry: Significance and Mitigation Strategy

Sami Samiei-Esfahany[1], **Pardis Ghobeiti-Nasab**✉[2]

1. School of Surveying and Geospatial Engineering, The University of Tehran, Tehran, Iran. E-mail: s.samieiesfahany@ut.ac.ir
2. Corresponding author, School of Surveying and Geospatial Engineering, The University of Tehran, Tehran, Iran. E-mail: Ghobeyti.pardis@ut.ac.ir

Article Info

Article type:
Research Article

Article history:
Received 2025-08-25
Received in revised form 20 December 2023
Accepted 2026-07-14
Available online 2026-07-24

Keywords:
InSAR,
Tropospheric Delay,
Anisotropic Turbulence,
Variogram Modelling,
Coastal Regions,
Atmospheric Corrections.

ABSTRACT

Tropospheric phase delays are a major source of error in interferometric synthetic aperture radar (InSAR) measurements, particularly in coastal areas with complex atmospheric dynamics. Traditional correction methods often assume isotropy in atmospheric turbulence, overlooking potential directional dependencies.

This study investigates the effectiveness of incorporating anisotropic models into tropospheric delay correction, focusing on geodynamically active coastal regions in southern Iran including the Makran coast, southern Zagros, and central Alborz as well as inland non-coastal areas such as South Khorasan.

An empirical variogram analysis of over 1,200 interferograms revealed significant directional dependence in tropospheric turbulence, most evident in coastal zones where moisture distribution and topography are highly heterogeneous. Among the tested variogram models exponential, Gaussian, and spherical, the exponential model consistently yielded the best fit, reducing the root mean square error (RMSE) by up to 57%.

Further evaluation using Least Squares Collocation (LSC) across four sampling scenarios demonstrated that anisotropic modeling significantly improves delay correction under sparse or irregular sampling conditions typical of coastal environments, achieving up to 15 cm improvement (50% RMSE reduction). In contrast, for densely and uniformly sampled regions, the gain was marginal (below 0.5 cm).

These findings underscore the importance of accounting for anisotropic atmospheric behavior in InSAR applications. The proposed anisotropic correction framework offers practical value for improving deformation monitoring in regions with challenging atmospheric conditions.

Cite this article: Samiei-Esfahany, S., Ghobeiti-Nasab, P. (2026). Anisotropic Behaviour of Atmospheric Disturbances in Coastal Areas for Satellite Radar Interferometry: Significance and Mitigation Strategy, *Earth Observation and Geomatics Engineering*, Volume 10, Issue 1, Pages 1-13. http//doi.org/10.22059/eoge.2026.400753.1188

Publisher: University of Tehran.
DOI: http//doi.org/10.22059/eoge.2026.400753.1188

1. Introduction

Interferometric Synthetic Aperture Radar (InSAR) is a remote sensing technique that measures Earth's surface deformations using phase information from repeated radar acquisitions (Gabriel et al., 1989). It provides millimetre-level precision, continuous large-scale monitoring, and the ability to operate in all weather conditions (Li et al., 2022; Massonnet & Feigl, 1998). However, the reliability and accuracy of InSAR measurements are primarily limited by atmospheric disturbances (Fattahi & Amelung, 2015), induced by spatial and temporal variations in pressure, temperature, and relative humidity in the troposphere (Hanssen, 1998).

Although advanced InSAR time-series methodologies, such as Persistent Scatterer Interferometry (PSI) and Small Baseline Subset (SBAS), have been developed over the years to enhance the accuracy InSAR deformation estimates by incorporating advanced atmospheric mitigation methods (Minh et al., 2022), atmospheric disturbances still remain as one of the most significant error sources for InSAR, especially for monitoring slow ground deformations. Therefore, any improvement in performance of these mitigation methods can directly contribute to the accuracy improvement of the InSAR-derived deformation products. One of the aspects of the common atmospheric mitigation methods is that these methods generally rely on the isotropic assumption, which posits that the spatial structure of turbulent delays depends solely on distance, neglecting directional variability or relying on overly simplified models (Agram & Simons, 2015; ZHAN et al., 2015). This study aims to assess the validity of this assumption.

Variations in tropospheric delay have been recognized as a major source of error in InSAR studies since the early days of the technique (Gabriel et al., 1989; Hanssen, 1998). Over the past three decades, various methods have been developed to suppress this noise. Different studies have categorized tropospheric errors into systematic and stochastic components, examining their behavior both spatially (Emardson et al., 2003; Hanssen, 2001) and temporally (Doin et al., 2009a; Fattahi & Amelung, 2015; Samsonov et al., 2014). Early methods relied on statistical techniques that assumed an uncorrelated random variation of the tropospheric phase in time. These include the pair-wise logic approach (Hanssen, 1998; Massonnet & Feigl, 1995), the stacking method (Emardson et al., 2003; Sandwell & Price, 1998), and widely adopted spatiotemporal filtering techniques (Ferretti et al., 2001; Schmidt et al., 2005; M. Wei et al., 2010), including low-pass filtering in time and different types of spatial filters (Ferretti et al., 2000; Hooper et al., 2007; Van Leijen, 2014). Though optimal performance of these kinds of methods requires a thorough analysis of the temporal and spatial properties of the atmosphere.

Advanced techniques utilize external data sources to estimate and mitigate tropospheric phase delays in InSAR observations. These sources include Global Positioning System (GPS) observations of zenith total delay (ZTD) (Löfgren et al., 2010; Onn & Zebker, 2006; Schmidt et al., 2005) and satellite observations, such as the Moderate Resolution Imaging Spectroradiometer (MODIS) and Medium Resolution Imaging Spectrometer (MERIS)(Li et al., 2005, 2006, 2009; Walters et al., 2013), as well as numerical weather models like ERA5 from the European Centre for Medium-Range Weather Forecasts (ECMWF) (Doin et al., 2009b; Jolivet et al., 2011, 2014; Liu et al., 2009; Walters et al., 2013) and the Generic Atmospheric Correction Online Service (GACOS) (Cao et al., 2018; Yu et al., 2017, 2018).

The use of additional data from GPS-derived tropospheric delay maps faces several limitations, including the limited availability of GPS stations, data inaccessibility in certain regions, and dependence on the accuracy of the underlying measurements (Chen et al., 2020). Similarly, numerical models encounter their own challenges, such as lower spatial resolution compared to radar data, discrepancies in model timing, and an inability to accurately capture localized atmospheric disturbances. These factors can hinder the effectiveness of both GPS data and numerical models in atmospheric correction (Hu et al., 2022; Kinoshita et al., 2013; Wadge et al., 2010).

Despite their limitations, these methods show some improvement in atmospheric correction but often assume isotropy in tropospheric turbulence. Early studies, however, pointed out its anisotropic nature. Hanssen (1998) (Hanssen, 1998) highlighted directional variability in tropospheric delays using variogram models, showing anisotropy's effect on phase measurements. Jonsson (2002) (Jonsson, 2002) refined these models, and Knospe and Jónsson (2010) (Knospe & Jonsson, 2009) introduced the Marten model, which improved correction accuracy in complex meteorological areas. Wei et al. (2019) (J. Wei et al., 2019) used exponential variograms to model anisotropy at various scales, revealing a combination of isotropic and anisotropic features in turbulence. These studies emphasize the importance of anisotropic modeling for accurate atmospheric corrections in InSAR.

In this research, we aim to address the following questions by analyzing the spatial behavior of the tropospheric turbulence phase and ultimately modeling its anisotropic characteristics.

- **Examining the Anisotropy of Tropospheric Delays in Coastal Areas.**
  - .1. Examination and analysis of the statistical characteristics of atmospheric errors, considering the hypothesis of anisotropy.
  - .2. What percentage of the interferograms generated from coastal areas in southern Iran exhibit anisotropic behavior in the atmospheric error component?
  - .3. What is the degree of anisotropy in atmospheric errors in coastal versus non-coastal regions, and how do their statistical behaviors compare?

- **Evaluating the Impact of the Anisotropy Assumption on Improving Atmospheric Correction**
  .1. Among the commonly used anisotropic statistical functions, which one offers the optimal performance for modeling atmospheric errors?
  .2. What effect does considering the tropospheric behavior as isotropic versus anisotropic have on the accuracy of the final phase prediction?

This paper is organized as follows: Section 2 introduces the theoretical framework of interferometric phase decomposition and atmospheric delay modeling. Section 3 describes the study areas, data, and empirical analysis of anisotropy. Section 4 presents scenario-based evaluations of anisotropic correction using Least Squares Collocation. Section 5 concludes with key findings and practical recommendations.

2. Investigation of Atmospheric Anisotropic Behavior in Coastal Areas

2.1. Interferometric phase

The interferometric phase (φ_{MS}) for a single pixel can be expressed as the sum of four components:

$$\varphi_{MS} = \varphi_{range} + \varphi_{Atmo} + \varphi_{Scat} + \varphi_{noise} \tag{1}$$

The range-dependent interferometric phase (φ_{range}), which corresponds to the distance between the radar sensor and the effective phase center of the resolution cell on the ground, can be further decomposed into three contributions: the flat Earth phase (φ_{flat}), the topographic phase (φ_{Topo}), and the deformation phase (φ_{def})(Esfahany, 2017).
It follows that:

$$\varphi_{MS} = \varphi_{flat} + \varphi_{topo} + \varphi_{def} + \varphi_{atmo} + \varphi_{scat} + \varphi_{noise} \tag{2}$$

The term φ_{atmo} represents the phase delay induced by atmospheric effects, while φ_{scat} corresponds to the scattering phase caused by the distribution of scatterers within a resolution cell. Additionally, φ_{noise} accounts for system-related or thermal noise, which depends on the sensor specifications.

Since our focus is on the atmospheric phase component, we aim to minimize the influence of other phase contributions. By selecting interferograms with small spatial and temporal baselines in non-deforming areas or areas with low deformation rates, the deformation phase (φ_{def}) can be considered negligible at each individual pixel. In this study, the interferograms were primarily generated using short temporal baselines (6–12 days), over which significant tectonic deformation is unlikely to occur. Therefore, the expected deformation signal is assumed to be substantially smaller than the atmospheric phase variations investigated in this work.

Next, to remove the flat Earth phase (φ_{flat}) and the topographic phase (φ_{topo}), we utilize precise orbit information, reference surface parameters, and an auxiliary digital elevation model (DEM), respectively. When removing φ_{flat}, a residual error may remain in the range-dependent phase. Errors and uncertainties in the precise orbit information lead to inaccuracies in the computation of the baseline parameter, introducing an additional phase component known as the orbital phase (φ_{orbit}). Thus, Equation (2) can be rewritten as:

$$\varphi_{MS} = \varphi_{orbit} + \varphi_{atmo} + \varphi_{scat} + \varphi_{noise} \tag{3}$$

The scattering phase is inherently a deterministic quantity, meaning that it remains unchanged under identical measurement conditions. However, it is unpredictable and cannot be modeled in a deterministic manner. When a resolution cell on the ground is observed by two radar antennas from different positions and, consequently, different incidence angles, the range distances of individual elementary scatterers within the cell to the two antennas vary. As a result, their phase contributions differ, leading to variations in the scattering phase between acquisitions.

The influence of the scattering phase is directly dependent on the baseline length. Thus, by carefully selecting interferograms with small spatial baselines, the impact of the scattering phase can be significantly reduced. In addition, the analysis in this study was restricted to high-coherence pixels and multi-looked observations, which further suppress decorrelation effects and random scattering-related phase noise. Since the primary focus of this work is on the long-wavelength behavior of atmospheric signals, the influence of scattering noise, which is generally spatially uncorrelated, is expected to be limited. Finally, owing to its spatially uncorrelated nature, the residual scattering noise appears as a nugget effect in the variogram analysis conducted in this study and, consequently, does not affect the estimated parameters of the atmospheric signal. Therefore, Equation (3) can be rewritten as:

$$\varphi_{MS} = \varphi_{orbit} + \varphi_{atmo} + \varphi_{noise} \tag{4}$$

As this study focuses solely on mitigating tropospheric delay, the physical characteristics of atmospheric delay will be analyzed in the following section.

2.2. Theory of atmospheric propagation delay

Since the atmospheric distribution varies over time, atmospheric delay is inevitable and can be expressed as(Hanssen, 2001) :

$$\tau(r) = \frac{1}{10^6 \cos(\theta)} \int_0^H N \, dz \tag{5}$$

Where $\tau(r)$ represents the atmospheric delay at pixel r in the line-of-sight (LOS) direction, while θ and H denote the radar incidence angle and satellite altitude, respectively.

Atmospheric refraction (N in Equation (5)) can be decomposed into two components: vertical stratification and horizontal turbulence (Hanssen, 2001). Consequently Equation (5) can be rewritten as:

$$\tau(r) = \frac{1}{10^{6}\cos(\theta)}\left\{\int_0^H N_{strat}\, dz + \int_0^H N_{turb}\, dz\right\} \qquad (6)$$

Where N_{strat} and N_{turb} represent the refractivity due to vertical stratification and horizontal turbulence, respectively.

2.3. Vertical stratified atmospheric delay in InSAR

The delay observed in differential interferometry arises from variations in the atmospheric path delay between two SAR acquisitions. Vertical stratification occurs due to differences in the tropospheric refraction profile at the times of the two SAR acquisitions. This effect primarily influences the refractive index in the vertical dimension.

If the atmosphere is modeled as a series of infinitesimally thin layers, each with a constant refractive index, the vertical delay between pixels p and q during acquisitions t_1 and t_2 can be expressed as (Hanssen, 2001):

$$\delta_{p,q}^{t_1}(h) = \int_p^q N^{t_1}(h)dh \qquad (7)$$

$$\delta_{p,q}^{t_2}(h) = \int_p^q N^{t_2}(h)dh \qquad (8)$$

Where N^{t_1} and N^{t_2} represent the refractivity at altitude H during epochs t_1 and t_2, respectively. Thus, the differential vertical delay is given by:

$$\Delta\delta_{p,q}^{t_1,t_2}(h) = \delta_{p,q}^{t_1}(h) - \delta_{p,q}^{t_2}(h) = \int_p^q (N^{t_1}(h) - N^{t_2}(h))dh \qquad (9)$$

This formulation indicates that the differential vertical delay is inherently dependent on the elevation of targets p and q. By integrating the vertical refractivity over varying altitudes, one can quantify the influence of tropospheric vertical stratification on the interferogram. However, estimating the vertical refractivity at each pixel in the InSAR interferogram remains challenging. Nevertheless, according to (Doin et al., 2009a). The stratification phase delay exhibits a linear decrease with elevation.

2.3. Turbulent mixing atmospheric delay in InSAR

The turbulent part of the troposphere is known as one of the main error sources in InSAR because of different turbulence processes occurring in this part. Unlike the vertical stratification delay, the turbulent delay is hard to describe using a deterministic model due to its random nature in both spatial and temporal domains (Li et al., 2022).

Regarding the temporal behavior, the turbulent mixing effect is generally only correlated in time on the scale of hours. As the time between two acquisitions in common SAR acquisitions is on the order of a couple of days to a month or more, the turbulent atmospheric signal can be considered effectively uncorrelated in time.

Based on Kolmogorov turbulence theory, the behavior of the interferometric turbulence signal is described as a spatially correlated stochastic process with a power-law behavior in space. In fact, for pixels with a short distance between them, the turbulent mixing phases are more similar. Based on this theory, it is commonly assumed that the turbulent atmosphere exhibits isotropic behavior. In order to evaluate the validity of this assumption, the anisotropic intensity will be studied using the variogram tool.

2.3. Variogram

Using a structure function or variogram is a common approach to characterize the turbulent mixing part of the atmosphere (Hanssen, 2001; J. Wei et al., 2019). The variogram is defined as:

$$\gamma(r) = \frac{1}{2}\left[\left(z(x_i) - z(x_i + r)\right)^2\right] \qquad (10)$$

Where z represents the observed samples, and r is the spatial distance, known as the lag. The variogram ($\gamma(r)$) in this equation depends on distance. To characterize the spatial structure of turbulent mixing delay directionally (north-south and east-west), it can be extended to two dimensions:

$$\gamma(r_x, r_y) = \frac{1}{2}\left[\left(z(x, y) - z(x + r_x, y + r_y)\right)^2\right] \qquad (11)$$

Where r_x and r_y are the lags along the east and north directions, respectively. When evaluating turbulent mixing in two directions, two scenarios can occur:

If the turbulent mixing exhibits different behavior in different directions, the variogram plot takes an elliptical shape, indicating geometric anisotropy.

To model the spatial structure of turbulent mixing, geometric anisotropy was considered. Therefore, a theoretical variogram model was selected from the variogram function sets presented by Goovaets (1997), and fitted using three common variogram models: exponential, Gaussian, and spherical variograms, while ensuring positive definiteness of the covariance structure, as shown in **Table (1).** While more flexible covariance models, such as the general Matérn or nested variogram formulations, may better capture multi-scale turbulent variability, the variogram models adopted in this study were found to provide a sufficiently accurate and computationally efficient representation of the dominant large-scale atmospheric correlation structures relevant to the analysis of anisotropic behavior.

In these functions, d represents the distance, and r is the correlation distance. Therefore, according to the assumption of geometric anisotropy, the ratio $(\frac{r}{d})$ in all the variogram functions is considered as:

$$\sqrt{\frac{\left(r_x \cos(\theta)+r_y \sin(\theta)\right)^2}{a_{max}}+\frac{\left(-r_x \sin(\theta)+r_{ycos(\theta)}\right)^2}{a_{min}}} \quad (12)$$

Where r_x and r_y represent the distances in the east-west and north-south directions, respectively; θ is the angle of deviation from the direction of maximum range a_{max}, and a_{min} are the highest and lowest ranges of correlation in the two mentioned directions. After assessing the compatibility of the proposed models, the turbulence phase will be predicted using the least squares collocation (LSC) method, with the model that demonstrates the highest compatibility.

Table (1). Autocorrelation and variogram functions for spatial models

Name	**Autocorrelation ($Q(r)$)-Variogram Functions ($\gamma(r)$)**
Exponential	$Q(r) = \sigma^2\left(e^{\frac{-d}{r}}\right)$ $\gamma(r) = \sigma^2(1 - e^{-\frac{d}{r}})$
Gaussian	$Q(r) = \sigma^2(e^{-\left(\frac{d}{r}\right)^2}$ $\gamma(r) = \sigma^2(1 - e^{-\left(\frac{d}{r}\right)^2})$
Spherical	$Q(r) = \sigma^2\left(1 - \frac{3}{2}\frac{d}{r} + \frac{1}{2}\left(\frac{d}{r}\right)^3\right), d \le r$ $Q(r) = 0\,, d > r$ $\gamma(r) = \sigma^2\left(\frac{3}{2}\frac{d}{r} - \frac{1}{2}\left(\frac{d}{r}\right)^3\right), d \le r$ $\gamma(r) = \sigma^2, d > r$

3. Study Areas and Data

To investigate the anisotropic behaviour of the turbulent component of the troposphere, five study regions, both coastal and non-coastal, were analysed. These include the Central Zagros (inland), Central Alborz (coastal), Southern Khorasan (inland), Southern Zagros (coastal), and the Western and Eastern Makran regions (coastal). The spatial distribution of these study areas is illustrated in **Figure (1)**.

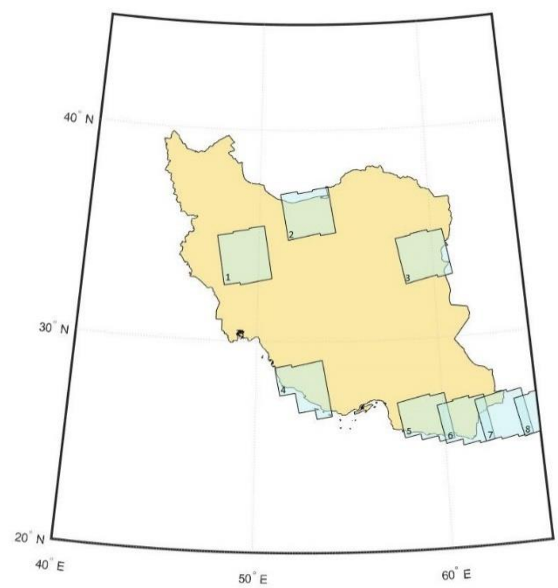

Figure (1). Study areas: 1. Middle Zagros (non-coastal), 2. Central Alborz (coastal), 3. South Khorasan (non-coastal), 4. South Zagros (coastal), 5. Western Makran (coastal), 6. Eastern Makran (coastal).

Among these regions, the Makran Coast has been designated as the primary study area due to its geodynamic complexity. Located at the boundary between the Arabian and Indian tectonic plates, this region is characterized by significant tectonic activity, necessitating precise atmospheric corrections to mitigate potential errors in interferometric analysis. The additional regions were selected to facilitate a comparative assessment of atmospheric behavior across distinct geological and climatic settings.

For this study, interferometric datasets were acquired from the School of Earth and Environment at the University of Leeds[1]. The dataset comprises 1200 interferograms, spanning the period from 2014 to 2022, with temporal baselines ranging from 6 to 12 days. These interferograms provide a robust foundation for analyzing atmospheric variability in the selected study areas.

To correct for atmospheric phase turbulence, the interferograms were processed using the Geocoded Atmospheric Correction for Synthetic Aperture Radar (GACOS) service, which offers high-resolution tropospheric corrections. The necessary atmospheric correction data were systematically retrieved and applied to each interferogram, ensuring a reliable statistical analysis. The corrected interferometric phase was subsequently used for detailed interpretation and comparative evaluation of atmospheric effects across the selected regions.

[1] https://comet.nerc.ac.uk/comet-lics-portal-velocities/

3.1. Phase Decomposition

As previously mentioned, factors such as a short temporal baseline (which leads to the omission of the displacement phase, (δ_{def}) and a short spatial baseline (resulting in the omission of the flat Earth phase, (δ_{flat}) help minimize the contribution of δ_{def} and δ_{flat} phases. Additionally, the utilization of a regional Digital Elevation Model (DEM) aids in accurately modelling the topographic phase and removing its effect from the interferometric phase (δ_{topo}). Consequently, the interferometric phase can be expressed as:

$$\psi_{ms} = \psi_{atmo} + \psi_{noise} \tag{13}$$

The atmospheric phase consists of two main components: the ionospheric phase and the tropospheric phase. The tropospheric phase, in turn, can be further divided into two parts: the stratified part and the turbulent part. Due to the strong correlation between the stratified component and topography, as well as the significant spatial correlation of ionospheric delays (which often exhibit behavior similar to orbital phase variations), a three-dimensional phase screen is employed to mitigate these effects.

In this study, a linear topography-dependent model was adopted to represent the stratified atmospheric component, as it provides a sufficient first-order approximation for isolating the dominant atmospheric behavior investigated here. Although higher-order or non-linear models may further improve atmospheric mitigation in operational applications, their influence on the anisotropic long-wavelength patterns analysed in this work is expected to be limited. The phase screen is represented as:

$$\psi_{SIO} = ax + by + ch + z \tag{14}$$

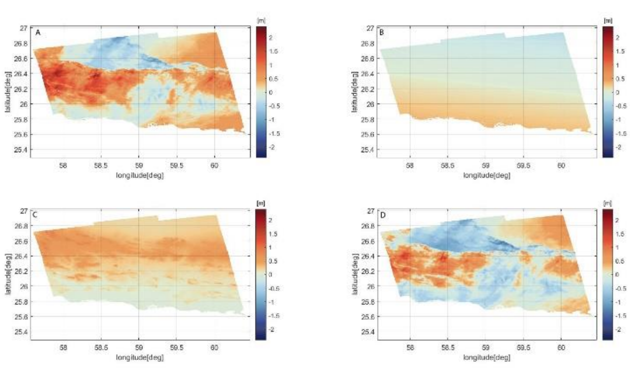

Figure (2). A: Interferometric Phase, B: Computed Trend, C: Stratified Layer Error obtained using the regional elevation model, D: Residual Phase after removing the trend and stratified layer error.

Here, ψ_{SIO} represents the combined contributions of stratification, ionospheric effects, and orbital errors. The coefficients a and b correspond to orbital error and ionospheric signal contributions, respectively, c accounts for the effects of the stratified layer, while z represents the reference latitude offset. The variables x,y, and h denote the geographic coordinates and altitude of each pixel within the study area.

This methodology was systematically applied to all interferograms analyzed in this study. A representative example of the process is illustrated in **Figure (2)**.

Several analytical approaches including power spectrum analysis, covariance functions, and variogram functions can be employed to investigate the behavior of the tropospheric turbulent layer. In this study, the variogram function is used as a statistical tool to characterize turbulence. The analysis begins with an empirical variogram assessment to examine the behavior of the turbulent layer in both the east-west and north-south directions. Subsequently, a robust model is developed to describe and quantify the observed phenomena.

3.2. Empirical Variogram

The differential variance (variogram) of turbulent phase measurements exhibits directional dependence when evaluated along the north–south and east–west orientations (**Figure (3)**). This directional variability reveals that the correlation between sample pairs is not uniform across these axes, a phenomenon known as anisotropy.

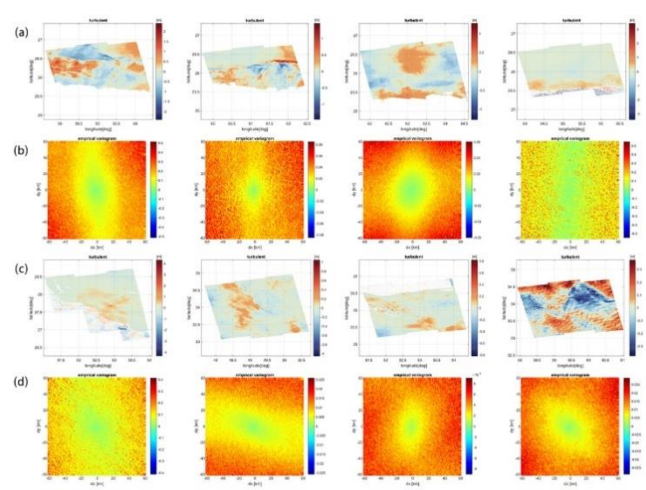

Figure (3). Rows (a) and (c) display the tropospheric turbulent phase. Rows (b) and (d) show the empirical variograms. In this figure, the signals presented in row (a) pertain to the coastal Makran region, while row (c) includes the other study areas.

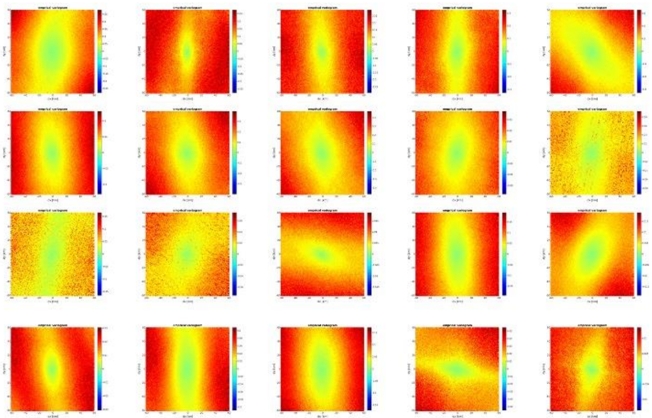

Figure (4). Displayed are 20 samples from the 1200 computed empirical variograms (units in square meters). The aim of this figure is to illustrate the directional behaviour of the tropospheric turbulent phase.

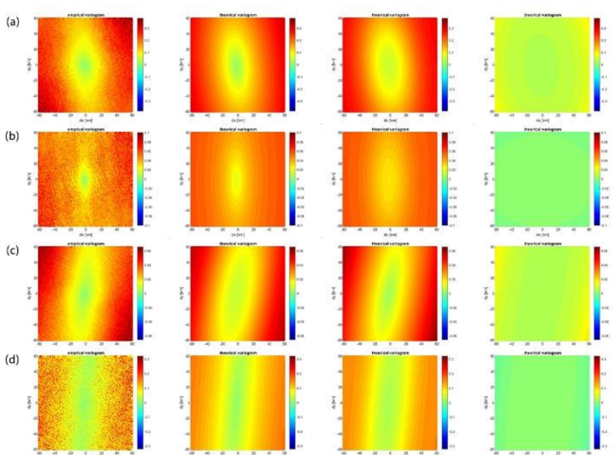

Figure (5). Empirical and modeled variograms (Exponential, Gaussian, Spherical) for interferograms from the coastal Makran region. Columns from left to right: Empirical, Exponential, Gaussian, and Spherical models.

Empirical variogram analysis consistently demonstrates directional characteristics, with varying degrees of anisotropy observed across different frames. Notably, the orientation and magnitude of anisotropy differ among individual interferograms. To systematically examine these variations, empirical variograms will be modeled under anisotropy assumptions. By computing the relevant anisotropy parameters, we aim to quantify both the extent and directional tendencies of anisotropy across multiple datasets.

3.3. Modelling of Anisotropic Variograms

Identifying the most suitable model for fitting the empirical variogram and accurately capturing its behavior is a challenging task. In this study, we employed three variogram models, exponential, Gaussian, and spherical to characterize the tropospheric turbulent phase. To illustrate the results, a random sample from each frame was selected and is presented in **Figures (5)** and (**6**).

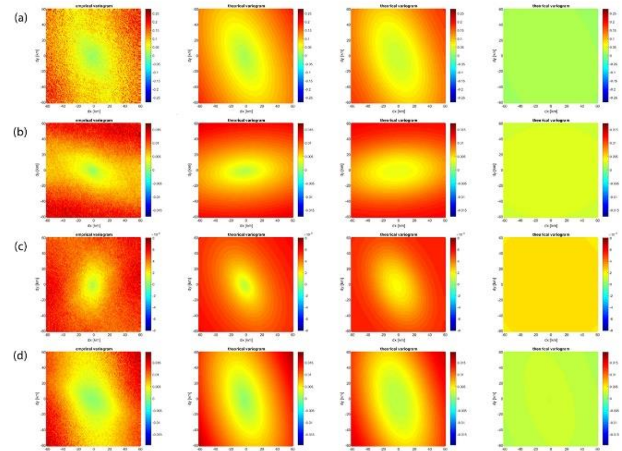

Figure (6). Empirical variogram and its exponential, Gaussian, and spherical fits for non-coastal interferograms. Columns (left to right): Empirical, Exponential, Gaussian, And Spherical.

To determine the most effective model for fitting the empirical variogram, we assessed the performance of each model using the root mean square error (RMSE). The model exhibiting the lowest RMSE and the best alignment with the empirical variogram was selected as the optimal model.

To quantify the degree of isotropy in the theoretical variograms, the isotropic ratio (IR) was introduced, defined as:

$$IR = \frac{R_2}{R_1}$$

Where R_1 and R_2 denote the maximum and minimum correlation lengths derived from the theoretical variogram, respectively. The isotropic ratio (IR) ranges between 0 and 1, where values approaching unity indicate an isotropic variogram and symmetrical turbulent behavior along the north-south and east-west directions.

To evaluate the effectiveness of the three modeling approaches, the average root mean square error (RMSE) was computed for each method across all frames, as depicted in **Figure (7)**.

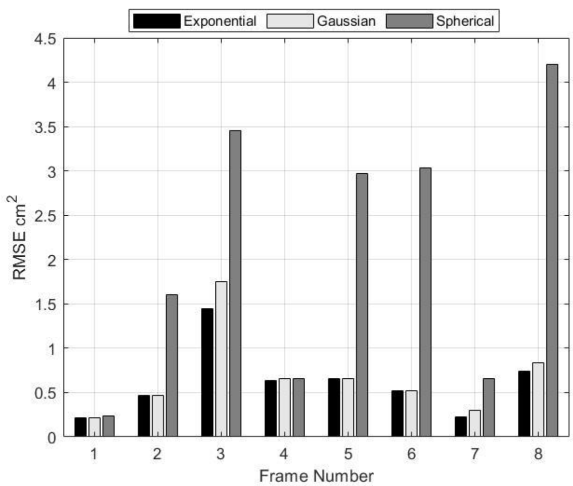

Figure (7). Theoretical variograms were fitted to 1200 interferograms using three models, exponential, Gaussian, and spherical. For each model, the root mean square error (RMSE) was computed per frame and then averaged across all frames to assess overall performance.

Table (2). Empirical variograms were modeled under anisotropic assumptions using exponential, Gaussian, and spherical functions. Comparative analysis based on frame-wise averaged RMSE values revealed that the exponential model consistently outperformed the other approaches, demonstrating superior fitting accuracy across all interferograms.

FN	Exp	Gaus	Sph
1	0.20	0.21	0.23
2	0.5	0.5	1.60
3	1.5	2	3.5
4	0.60	0.60	0.65
5	0.65	0.70	3
6	0.50	0.50	3
7	0.20	0.20	0.65
8	1	1	4

To gain a deeper understanding of the extent of anisotropy in the coastal Makran region, which includes over 800 interferograms, a histogram is utilized for a more detailed analysis (**Figure (8)**).

Table (3). On average, the exponential variogram model achieved a 56% improvement in RMSE compared to the spherical model and a 4% improvement relative to the Gaussian model, confirming its superior performance in capturing anisotropic atmospheric behaviour.

FN	Impro (Exp/ Gau) %	Impro (Exp/Sph) %
1	5	13
2	4	71
3	16.5	58
4	4.5	3
5	6	78
6	0.2 (< 1)	83
7	4	66
8	11	82

Although the exponential and Gaussian functions produce closely comparable results, the exponential function consistently outperforms both the spherical and Gaussian models across the majority of study frames (numerical results are provided in **Table (2)**). Furthermore, as summarized in **Table (3)**, when averaged over all frames, the exponential function demonstrates a 56% improvement relative to the spherical function and a 4% improvement compared to the Gaussian function.

To assess anisotropy in each interferogram, the isotropy ratio derived from the exponential model was employed (see **Table (4)**). This table provides the average isotropy ratio calculated for all interferograms within each frame. The results clearly demonstrate that coastal regions exhibit lower isotropy ratios, signifying higher levels of anisotropy in these areas.

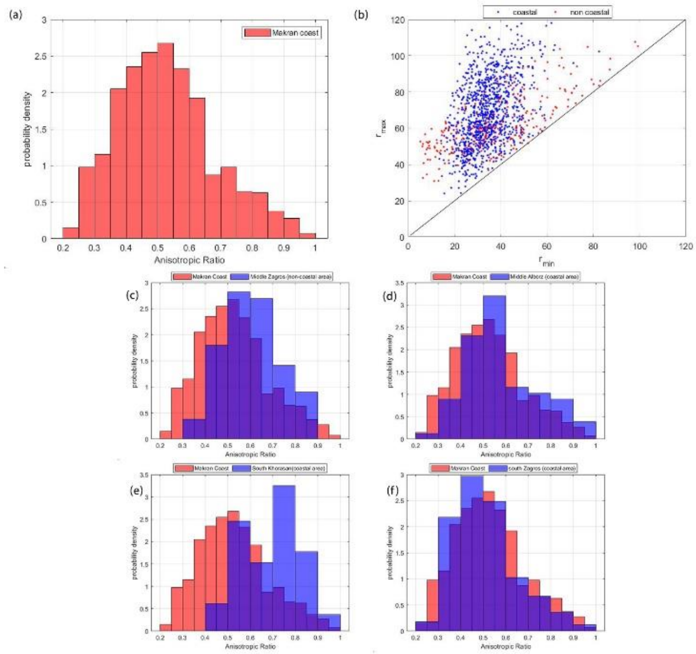

Figure (8). (a) Isotropy ratio distribution in the coastal Makran region (x-axis: maximum correlation, y-axis: minimum correlation). (b–f) Comparative analysis of isotropy ratios between Makran and other regions: Central Alborz, Southern Zagros, and non-coastal areas (Frames 1–3). Results show ~5% higher anisotropy in coastal regions relative to inland areas.

The histograms shown in **Figure (8)** reveal the presence of anisotropy across all regions, with a more pronounced effect observed in coastal areas compared to non-coastal regions. This increased anisotropy in coastal regions can be attributed to several factors, including the moisture content from the proximity to the sea and the significant topographic variation along the coastline.

4. Refining Tropospheric Corrections via Anisotropic Assumption

In this section, the Least-Squares Collocation (LSC) method is applied to predict tropospheric delays. This is done using four scenarios of coastal and non-coastal interferometric datasets, which are characterized by varying spatial scales and observation densities. The designed scenarios reflect realistic sampling densities and spatial distributions encountered in InSAR observations while providing a controlled framework for systematically evaluating the impact of sampling density and spatial heterogeneity on anisotropic atmospheric behavior.

4.1. Scenario 1: Uniform and Sparse Sampling in a Coastal Region

In this scenario, interferograms from Frame 5 over the Makran coast were used to predict tropospheric delays under homogeneous sampling. Both isotropic and anisotropic models were tested.

The anisotropic model significantly outperformed the isotropic one, yielding an average RMSE reduction of approximately 20 cm, which corresponds to ~40% decrease from the isotropic model's RMSE. Here, relative improvement is defined as the percentage reduction in RMSE:

$$Improvment\ (\%) = \frac{RMSE_{Isotropic} - RMSE_{Anisotropic}}{RMSE_{Isotropic}} \times 100$$

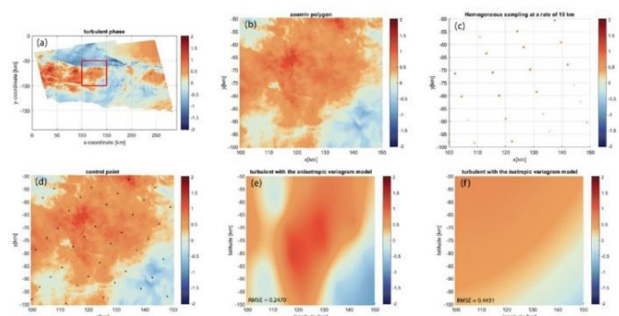

Figure (9). (a) Tropospheric turbulence phase and delineated study area, (b) magnified view of the selected region, (c) observation points at 10 km sampling intervals, (d) control points, (e) predicted tropospheric turbulence phase under the anisotropic model (RMSE shown, units in meters), (f) predicted tropospheric turbulence phase under the isotropic model (units in meters).

Table (4). Average isotropy ratios derived from the exponential model are reported per frame. Coastal frames (1, 4–8) exhibit lower isotropy ratios, indicating stronger anisotropic behavior compared to non-coastal regions.

FN	IR	FN	IR
1	0.6505	5	0.5063
2	0.7123	6	0.6009
3	0.6509	7	0.5812
4	0.5051	8	0.5012

4.2. Scenario 2: Uniform and Dense Sampling in a Coastal Region

Here, tropospheric phase delays from interferograms over the Makran coastal region were predicted using both isotropic and anisotropic models. Under dense sampling conditions, the difference between the two assumptions was minimal. The isotropic model yielded an average RMSE of approximately 12.5 cm. The anisotropic model reduced the RMSE by about 0.2 cm, corresponding to an improvement of ~2% relative to the isotropic baseline.

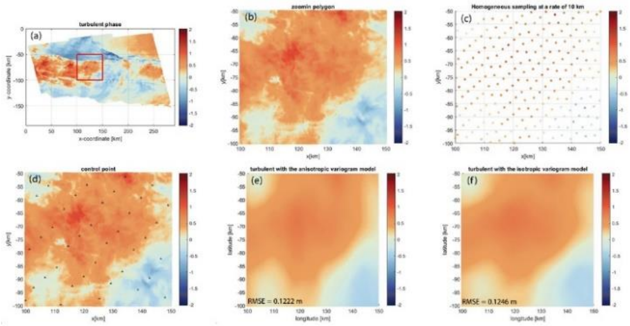

Figure (10). (a) Tropospheric turbulence phase and delineated region, (b) magnified view of the delineated area, (c) observation points with a sampling interval of 5 km, (d) Control points, (e) predicted tropospheric turbulence phase under the anisotropic assumption, (f) predicted tropospheric turbulence phase under the isotropic assumption.

4.3. Scenario 3: Uniform and Moderately Dense Sampling in a Non-Coastal Area

In this scenario, tropospheric phase delays over the inland region of South Khorasan were analyzed. Based on the RMSE values, only a marginal difference was observed between the isotropic and anisotropic models. The latter showed a slight improvement in accuracy of around 0.4 cm, corresponding to less than 1% average enhancement.

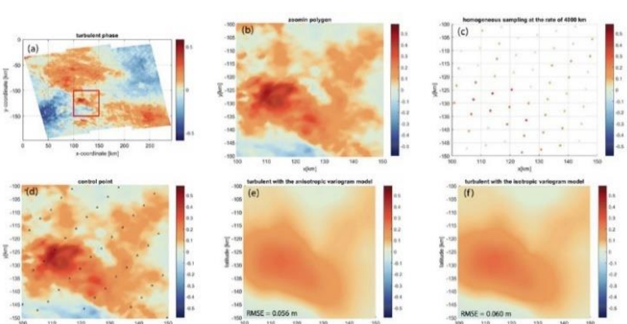

Figure (11). (a) Tropospheric turbulence phase and delineated region, (b) magnified view of the delineated area, (c) observation points with a sampling interval of 4 km, (d) control points, (e) predicted tropospheric turbulence phase under the anisotropic assumption, (f) predicted tropospheric turbulence phase under the isotropic assumption.

4.4. Scenario 4: Heterogeneous Sampling in a Coastal Region

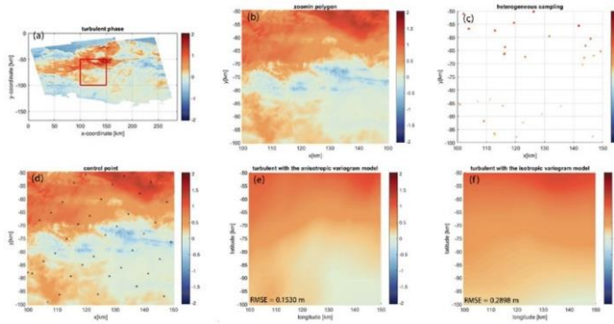

Figure (12). (a) Tropospheric turbulence phase and delineated region;(b) magnified view of the delineated area, (c) observation points with a sampling interval of 5 km, (d) control points, (e) predicted tropospheric turbulence phase under the anisotropic assumption, (f) predicted tropospheric turbulence phase under the isotropic assumption.

In this scenario, another frame from the Makran coastal region was analyzed, with observational samples selected at low and uneven density.

Under heterogeneous sampling particularly in Makran coastal region, the anisotropic approach achieved the greatest improvement observed in this study, with an average RMSE reduction of approximately 15 cm or ~50% enhancement.

This study evaluated the impact of anisotropic assumptions on tropospheric delay correction across four distinct sampling scenarios involving both coastal and inland interferograms. Prediction experiments were performed using both isotropic and anisotropic models on 50 interferograms from the Makran coast, southern Zagros, and central Alborz regions.

In all cases, the anisotropic model consistently outperformed the isotropic one. However, the extent of improvement depended strongly on the sampling configuration. Under sparse or heterogeneous sampling, particularly in coastal regions, the anisotropic approach achieved the highest improvement among all scenarios, with an average RMSE reduction of approximately 15 cm (~50%). In contrast, for dense and uniform sampling, the performance difference was minimal, often below ~0.5 cm. In such cases, the isotropic model may serve as a computationally efficient alternative with acceptable accuracy.

What these results highlight is that both the regional climate and the spatial density of observations govern how accurately tropospheric phase delays can be predicted. In practice, anisotropic modelling becomes especially valuable in two common situations: humid coastal environments, where atmospheric anisotropy is inherently strong, and settings where measurements are sparse or unevenly distributed, for example, surveys that lack dense ground control or face irregular acquisition geometries, where isotropic assumptions may introduce notable bias. In contrast, isotropic models may remain sufficient in dense and spatially uniform settings, particularly when atmospheric variability exhibits limited directional dependence. Such conditions are widespread in real-world InSAR applications, including land subsidence monitoring, earthquake deformation analysis, and infrastructure stability assessment.

5. Conclusion and Recommendations

This study aimed to investigate the role of anisotropic assumptions in improving tropospheric delay corrections, particularly in coastal and non-coastal regions of Iran. Over 1,200 interferograms from six geodynamically and climatologically diverse areas including western and eastern Makran, southern Zagros, central Alborz, and South Khorasan were analyzed.

Using empirical variograms along east–west and north–south directions, significant anisotropic behavior was observed in all regions, especially in coastal areas. Anisotropic modeling using exponential variogram functions consistently outperformed isotropic approaches, achieving up to 57% lower RMSE in model fitting. The severity of anisotropy was strongly correlated with environmental moisture and proximity to the sea.

To evaluate the impact of anisotropy on actual delay correction, the Least-Squares Collocation method was implemented across four synthetic scenarios using both isotropic and anisotropic models. The results showed that:

- In sparse or heterogeneous sampling conditions, anisotropic modeling significantly improved correction accuracy up to approximately 15 cm or about 50% improvement.

- In dense and uniform sampling scenarios, the difference was negligible less than 0.5 cm, or around 2%.

Ultimately, anisotropy was found to be a critical factor in tropospheric delay correction, especially in low-density or anisotropically distributed datasets. Based on these findings, we recommend applying anisotropic modeling in regions with sparse observations or complex topography. Although anisotropic approaches require the estimation of directional covariance structures and multi-directional variograms, isotropic assumptions may remain sufficiently accurate and computationally efficient in regions characterized by dense observations and relatively homogeneous spatial conditions. In practice, however, the additional computational burden of anisotropic modeling is relatively small compared with the overall computational requirements of InSAR time-series analysis. Therefore, when directional atmospheric variability is present, the improvement in modeling accuracy often outweighs the modest increase in computational cost. Future studies are encouraged to incorporate meteorological models to validate and compare estimated delays against physically simulated atmospheric fields. In addition, future investigations may benefit from the development of more comprehensive anisotropy metrics and generalized formulations of the anisotropy ratio for a more detailed characterization of atmospheric turbulence behavior.

References

Fattahi, H., & Amelung, F. (2015). InSAR observations of strain accumulation and fault creep along the Chaman fault system, Pakistan and Afghanistan. *Geophysical Research Letters, 42*(14), 5736–5743. https://doi.org/10.1002/2015GL064424

Gabriel, A. K., Goldstein, R. M., & Zebker, H. A. (1989). Mapping small elevation changes over large areas: Differential radar interferometry. *Journal of Geophysical Research: Solid Earth, 94*(B7), 9183–9191. https://doi.org/10.1029/JB094iB07p09183

Hanssen, R. F. (1998). Atmospheric heterogeneities in interferometric SAR. *European Space Agency, (Special Publication), 1*, 525–530.

Li, Z., Lv, L., Yang, Y., & Hoey, T. (2022). Atmospheric correction of InSAR data: Review, challenges and opportunities. *Remote Sensing of Environment, 268*, 112778. https://doi.org/10.1016/j.rse.2021.112778

Massonnet, D., & Feigl, K. L. (1998). Radar interferometry and its application to changes in the Earth's surface. *Reviews of Geophysics, 36*(4), 441–500. https://doi.org/10.1029/97RG03139

Agram, P. S., & Simons, M. (2015). A noise model for InSAR time series. *Journal of Geophysical Research: Solid Earth, 120*(4), 2752–2771. https://doi.org/10.1002/2014JB011271

Cao, Y., Li, Z., Wei, J., Hu, J., Duan, M., & Feng, G. (2018). Stochastic modeling for time series InSAR: With emphasis on atmospheric effects. *Journal of Geodesy, 92*, 185–204. https://doi.org/10.1007/s00190-017-1055-x

Chen, Y., Bruzzone, L., Jiang, L., & Sun, Q. (2020). ARU-net: Reduction of atmospheric phase screen in SAR interferometry using attention-based deep residual U-net. *IEEE Transactions on Geoscience and Remote Sensing, 59*(7), 5780–5793. https://doi.org/10.1109/TGRS.2020.2989286

Doin, M.-P., Lasserre, C., Peltzer, G., Cavalié, O., & Doubre, C. (2009a). Corrections of stratified tropospheric delays in SAR interferometry: Validation with global atmospheric models. *Journal of Applied Geophysics, 69*(1), 35–50. https://doi.org/10.1016/j.jappgeo.2009.02.001

Doin, M.-P., Lasserre, C., Peltzer, G., Cavalié, O., & Doubre, C. (2009b). Corrections of stratified tropospheric delays in SAR interferometry: Validation with global atmospheric models. *Journal of Applied Geophysics, 69*(1), 35–50. https://doi.org/10.1016/j.jappgeo.2009.02.001

Emardson, T. R., Simons, M., & Webb, F. H. (2003). Neutral atmospheric delay in interferometric synthetic aperture radar applications: Statistical description and mitigation. *Journal of Geophysical Research: Solid Earth, 108*(B5), 2282. https://doi.org/10.1029/2002JB001781

Fattahi, H., & Amelung, F. (2015). InSAR bias and uncertainty due to the systematic and stochastic tropospheric delay. *Journal of Geophysical Research: Solid Earth, 120*(12), 8758–8773. https://doi.org/10.1002/2015JB012095

Ferretti, A., Prati, C., & Rocca, F. (2000). Nonlinear subsidence rate estimation using permanent scatterers in differential SAR interferometry. *IEEE Transactions on Geoscience and Remote Sensing, 38*(5), 2202–2212. https://doi.org/10.1109/36.868878

Ferretti, A., Prati, C., & Rocca, F. (2001). Permanent scatterers in SAR interferometry. *IEEE Transactions on Geoscience and Remote Sensing, 39*(1), 8–20. https://doi.org/10.1109/36.898661

Gabriel, A. K., Goldstein, R. M., & Zebker, H. A. (1989). Mapping small elevation changes over large areas: Differential radar interferometry. *Journal of Geophysical Research: Solid Earth, 94*(B7), 9183–9191. https://doi.org/10.1029/JB094iB07p09183

Hanssen, R. F. (1998). Atmospheric heterogeneities in interferometric SAR. *European Space Agency, (Special Publication), 1*, 525–530.

Hanssen, R. F. (2001). *Radar interferometry: Data interpretation and error analysis* (Vol. 2). Springer. https://doi.org/10.1007/0-306-47633-9

Hooper, A., Segall, P., & Zebker, H. A. (2007). Persistent scatterer interferometric synthetic aperture radar for crustal deformation analysis, with application to Volcán Alcedo, Galápagos. *Journal of Geophysical Research: Solid Earth, 112*(B7), B07407. https://doi.org/10.1029/2006JB004763

Hu, F., Helfer, K. C., Siebesma, A. P., & Hanssen, R. F. (2022). On the value of LES models for evaluating spatio-temporal tropospheric variability in multitemporal SAR interferograms. *IEEE Journal of Selected Topics in Applied Earth Observations and Remote Sensing, 15*, 7088–7099. https://doi.org/10.1109/JSTARS.2022.3195478

Jonsson, S. (2002). Modeling volcano and earthquake deformation from satellite radar interferometric observations. PhD thesis, Stanford University.

Jolivet, R., Grandin, R., Lasserre, C., Doin, M.-P., & Peltzer, G. (2011). Systematic InSAR tropospheric phase delay corrections from global meteorological reanalysis data. *Geophysical Research Letters, 38*(17), L17311. https://doi.org/10.1029/2011GL047084

Jolivet, R., Agram, P. S., Lin, N. Y., Simons, M., Doin, M.-P., Peltzer, G., & Li, Z. (2014). Improving InSAR geodesy using global atmospheric models. *Journal of Geophysical Research: Solid Earth, 119*(3), 2324–2341. https://doi.org/10.1002/2013JB010807

Kinoshita, Y., Furuya, M., Hobiger, T., & Ichikawa, R. (2013). Are numerical weather model outputs helpful to reduce tropospheric delay signals in InSAR data. *Journal of Geodesy, 87*, 267–277. https://doi.org/10.1007/s00190-012-0596-x

Knospe, S., & Jonsson, S. (2009). Covariance estimation for dInSAR surface deformation measurements in the presence of anisotropic atmospheric noise. *IEEE Transactions on Geoscience and Remote Sensing, 48*(4), 2057–2065. https://doi.org/10.1109/TGRS.2009.2013246

Li, Z., Cao, Y., Wei, J., Duan, M., Wu, L., Hou, J., & Zhu, J. (2019). Time-series InSAR ground deformation monitoring : Atmospheric delay modeling and estimating. *Earth-Science Reviews, 192*, 258–284. https://doi.org/10.1016/j.earscirev.2019.02.016

Li, Z., Duan, M., Cao, Y., Mu, M., He, X., & Wei, J. (2022). Mitigation of time-series InSAR turbulent atmospheric phase noise: A review. *Geodesy and Geodynamics, 13*(2), 93–103. https://doi.org/10.1016/j.geog.2021.12.002

Li, Z., Fielding, E., Cross, P., & Preusker, R. (2009). Advanced InSAR atmospheric correction: MERIS/MODIS combination and stacked water vapour models. *International Journal of Remote Sensing, 30*(13), 3343–3363. https://doi.org/10.1080/01431160802549191

Li, Z., Fielding, E. J., Cross, P., & Muller, J.-P. (2006). Interferometric synthetic aperture radar atmospheric correction: Medium resolution imaging spectrometer and advanced synthetic aperture radar integration. *Geophysical Research Letters, 33*(6), L06403.

https://doi.org/10.1029/2005GL025397

Li, Z., Muller, J.-P., Cross, P., & Fielding, E. J. (2005). Interferometric synthetic aperture radar (InSAR) atmospheric correction: GPS, Moderate Resolution Imaging Spectroradiometer (MODIS), and InSAR integration. *Journal of Geophysical Research: Solid Earth, 110*(B3), B03410. https://doi.org/10.1029/2004JB003536

Liu, S., Hanssen, R., & Mika, Á. (2009). On the value of high-resolution weather models for atmospheric mitigation in SAR interferometry. In *IGARSS 2009 IEEE International Geoscience and Remote Sensing Symposium* (Vol. 2, pp. II-749–II-752). https://doi.org/10.1109/IGARSS.2009.5418043

Löfgren, J. S., Björndahl, F., Moore, A. W., Webb, F. H., Fielding, E. J., & Fishbein, E. F. (2010). Tropospheric correction for InSAR using interpolated ECMWF data and GPS zenith total delay from the Southern California integrated GPS network. In *IGARSS 2010 IEEE International Geoscience and Remote Sensing Symposium* (pp. 4503–4506). https://doi.org/10.1109/IGARSS.2010.5654085

Minh, D. H. T., Hanssen, R., Doin, M.-P., & Pathier, E. (2022). Advanced methods for time-series InSAR. In *IGARSS 2022–2022 IEEE International Geoscience and Remote Sensing Symposium* (pp. 2854–2857). https://doi.org/10.1109/IGARSS46834.2022.9883912

Onn, F., & Zebker, H. A. (2006). Correction for interferometric synthetic aperture radar atmospheric phase artifacts using time series of zenith wet delay observations from a GPS network. *Journal of Geophysical Research: Solid Earth, 111*(B9), B09408. https://doi.org/10.1029/2005JB004012

Samsonov, S. V., Trishchenko, A. P., Tiampo, K., González, P. J., Zhang, Y., & Fernández, J. (2014). Removal of systematic seasonal atmospheric signal from interferometric synthetic aperture radar ground deformation time series. *Geophysical Research Letters, 41*(17),6123–6130. https://doi.org/10.1002/2014GL061658

Sandwell, D. T., & Price, E. J. (1998). Phase gradient approach to stacking interferograms. *Journal of Geophysical Research: Solid Earth, 103*(B12), 30183–30204. https://doi.org/10.1029/98JB02408

Schmidt, D., Bürgmann, R., Nadeau, R., & d'Alessio, M. (2005). Distribution of aseismic slip rate on the Hayward fault inferred from seismic and geodetic data. *Journal of Geophysical Research: Solid Earth, 110*(B8), B08409. https://doi.org/10.1029/2004JB003493

Van Leijen, F. J. (2014). Persistent scatterer interferometry based on geodetic estimation theory (Doctoral dissertation, TU Delft, Delft University of Technology). https://doi.org/10.4233/uuid:5dba48d7-ee26-4449-b674-caa8df93e71e

Walters, R., Elliott, J., Li, Z., & Parsons, B. (2013). Rapid strain accumulation on the Ashkabad fault (Turkmenistan) from atmosphere-corrected InSAR. *Journal of Geophysical Research: Solid Earth, 118*(7), 3674–3690. https://doi.org/10.1002/jgrb.50236

Wadge, G., Zhu, M., Holley, R., James, I., Clark, P., Wang, C., & Woodage, M. (2010). Correction of atmospheric delay effects in radar interferometry using a nested mesoscale atmospheric model. *Journal of Applied Geophysics, 72*(2), 141–149. https://doi.org/10.1016/j.jappgeo.2010.08.003

Wei, J., Li, Z., Hu, J., Feng, G., & Duan, M. (2019). Anisotropy of atmospheric delay in InSAR and its effect on InSAR atmospheric correction. *Journal of Geodesy, 93*(2), 241–265. https://doi.org/10.1007/s00190-018-1155-x

Yu, C., Li, Z., Penna, N. T., & Crippa, P. (2018). Generic atmospheric correction model for interferometric synthetic aperture radar observations. *Journal of Geophysical Research: Solid Earth, 123*(10), 9202–9222. https://doi.org/10.1029/2018JB016385

Yu, C., Penna, N. T., & Li, Z. (2017). Generation of real-time mode high-resolution water vapor fields from GPS observations. *Journal of Geophysical Research: Atmospheres, 122*(3), 2008–2025. https://doi.org/10.1002/2016JD025753

ZHAN, W.-J., LI, Z.-W., WEI, J.-C., ZHU, J.-J., & WANG, C.-C. (2015). A strategy for modeling and estimating atmospheric phase of SAR interferogram. *Chinese Journal of Geophysics, 58*(7), 2320–2329. https://doi.org/10.6038/cjg20150727

Agram, P. S., & Simons, M. (2015). A noise model for InSAR time series. *Journal of Geophysical Research: Solid Earth, 120*(4), 2752–2771. https://doi.org/10.1002/2014JB011271